

Nucleation bursts of primary intermetallic crystals in a liquid Al alloy studied using *in situ* synchrotron X-ray radiography

Shikang Feng ^{*1}, Enzo Liotti¹, Andrew Lui¹, Matthew D. Wilson², and Patrick S. Grant¹

¹*Department of Materials, University of Oxford, Oxford, OX1 3PH, UK*

²*Science and Technology Facilities Council, Rutherford Appleton Laboratory, Harwell Science and Innovation Campus, Didcot, OX11 0DE, UK*

Abstract

The nucleation of primary Pt-rich intermetallic compound (IMC) crystals was studied in a model Al-Pt-Er alloy as an analogue to $\text{Al}_{13}\text{Fe}_4$ that forms in commercial Al alloys. The Pt-rich IMCs provided strong X-ray absorption contrast that allowed earlier detection of formation events and the resolution of solute diffusion fields. Crystal formation behaviour was investigated during directional and isothermal solidification when the alloy was inoculated with TiB_2 particles at cooling rates of 0.1 Ks^{-1} to 8 Ks^{-1} using *in situ* synchrotron X-ray radiography. Different from previous studies that concerned disordered, solid solution phases such as α -Al dendrites, for the first time nucleation bursts of ordered compound crystals were observed, where the nucleation of the IMC crystals proceeded in distinct cascades (in the time domain) or waves (in the spatial domain), the magnitude of which increased with increasing cooling rate and particularly with decreasing thermal gradient in the melt. Comparing the crystal number density with the estimated number density of TiB_2 particles suggested that the IMC crystals nucleated only on the most potent TiB_2 particles, accounting for $\sim 0.5\%$ of the total TiB_2 number density in the melt. The effect of the thermal gradient and cooling rate on the magnitude of the nucleation waves and the IMC number density was revealed in terms of the available undercooling in the liquid in front of an individual IMC and the solute depleted liquid fraction that arose from the interaction of an ensemble of IMC crystals.

Keywords: *Primary intermetallics; Nucleation bursts; Available undercooling; In situ X-ray radiography; Al alloys*

*Corresponding author.

Email address: shikang.feng@materials.ox.ac.uk (S. Feng).

1 Introduction

During the cooling of a liquid metallic alloy, transformation from liquid to solid starts with the nucleation and formation of solid crystals at a temperature below the equilibrium melting temperature of the alloy, and this is followed by crystal growth, which may or may not be accompanied by further crystal formation events. The promotion or suppression of crystal nucleation plays a critical role in controlling the final crystal (or grain) size, distribution and morphology, and thus microstructure and mechanical properties of engineering alloy products, such as aluminium alloys and magnesium alloys used for automotive components, and nickel-based alloys used for turbine blades. In the aluminium industry, the nucleation of the α -Al grains that comprise >95 vol% of the final microstructure is promoted by inoculation with insoluble grain refiner particles such as TiB_2 and TiC . Inoculation results in a finer grain size and better, more isotropic mechanical properties [1]. A number of models of how these “extrinsic” additions promote nucleation have been developed since the middle of the last century [2–11].

With the advent of the high-energy, high-brilliance third-generation synchrotrons, and the development of better laboratory-based X-ray sources, *in situ* X-ray imaging techniques, such as radiography and tomography, have been used increasingly to investigate alloy solidification. The majority of these studies have focused on crystal growth of the primary α -Al phase, including the morphological instability of the growing solid/liquid interface [12, 13], columnar-to-equiaxed transition [14–16], dendrite fragmentation [17–20] and growth velocity of equiaxed dendrites [21–23]. In contrast, only a handful of studies have concerned crystal nucleation or the moment of crystal formation, principally due to the difficulties of imaging tiny nucleants and embryonic crystals.

Waves of equiaxed α -Al dendrite formation were first reported by Prasad *et al.* in Al-Si alloys [24] and by Jia *et al.* in an Al-Cu alloy [25]. Building on these qualitative insights, Liotti *et al.* combined X-ray radiography with machine learning and investigated the effect of alloy composition, cooling rate and instantaneous local

30 solute concentration on the nucleation of equiaxed α -Al dendrites in Al-Cu alloys
at cooling rates of 0.3 Ks^{-1} to 1.5 Ks^{-1} [26]. Using a “reverse time” approach,
they measured the instantaneous Cu concentration in the local region just before
a new α -Al dendrite appeared at that point, and estimated the undercooling of
over 14,000 grain formation events. Using a time series analysis of all these data,
35 they showed unambiguously that new crystals formed in distinct waves rather than
semi-continuously, and that these waves were associated with higher undercoolings
that enhanced the efficiency of crystal formation, and led to a finer grain size [26].

Aside from considering the majority, solid solution α -Al phase, studying *in situ*
the nucleation of the minority, ordered intermetallic compounds (IMCs), which are
40 an important feature of most Al alloys (e.g. Fe-rich IMCs), presents particular chal-
lenges because of their low volume fraction ($<2\%$). Fe-rich IMCs, such as $\text{Al}_{13}\text{Fe}_4$,
may grow into coarse ($\sim 10 \text{ }\mu\text{m}$ to several millimetres [27]), plate-like secondary
phases in both cast and wrought alloys, and can act as strain concentrators that
undermine alloy ductility and toughness [28, 29]. Feng *et al.* used both synchrotron
45 and laboratory X-ray facilities to investigate the formation of primary $\text{Al}_{13}\text{Fe}_4$ IMCs
in a hypereutectic Al-3Fe (wt%) alloy, along with the effect of TiB_2 and TiC inocula-
tion under both directional and near-isothermal solidification conditions [30]. Based
on over 4,500 crystal formation events, they showed that TiB_2 and TiC - normally
added to promote α -Al grain formation - also consistently increased the number
50 density and formation rate of primary $\text{Al}_{13}\text{Fe}_4$ crystals under all solidification con-
ditions. However, due to limitations in X-ray absorption contrast, spatial-temporal
resolution and image quality in the experiments, resolving the very earliest stages of
faceted crystal formation and time-resolved quantification of crystal formation rate
was not possible, and thus there were no insights regarding any nucleation bursts
55 in the temporal domain [30].

In this paper, to understand better ordered IMC formation behaviour, especially
in the temporal domain, we investigate the formation of primary IMC crystals in
a model Al-Pt-Er ternary alloy. This unusual composition alloy is at first consid-
eration an odd choice, but is carefully designed because it not only forms faceted,

plate-like Pt-rich IMCs that are morphologically closely related to $\text{Al}_{13}\text{Fe}_4$, but critically it also provides very strong X-ray absorption contrast between the Pt-rich IMCs and the Pt-depleted surrounding liquid that facilitates the resolution and analysis of the crystal formation stage and the associated diffusion field. More details behind the alloy choice are given later. We resolve and analyse 4,037 IMC nucleation events and show that the nucleation of the primary IMC crystals occurs in distinct waves, and that the magnitude of the waves increases with increasing cooling rate and is particularly sensitive to thermal gradient. For a given thermal gradient, the final IMC number density first increases rapidly as cooling rate increases from 0.1 Ks^{-1} to 0.5 Ks^{-1} , but then levels off up to 8 Ks^{-1} . The role of cooling rate and thermal gradient on the nucleation bursts, and therefore the final IMC number density is related to the magnitude of liquid undercooling around individual pre-existing IMCs. Then, by considering the interaction between an ensemble of IMCs and potential nucleants, and using the time-resolved measurement of the Pt-depletion liquid fraction, we show that the probability of IMC nucleation at any instant depends on the number of pre-existing IMCs and the liquid fraction in the environment that is solute depleted, which in turn depends on macro-scale cooling rate and thermal gradient conditions. Finally, the implications for commercial castings are considered.

2 Experimental methods

2.1 Alloy selection

An alloy composition of Al-23Pt-20Er (wt%) with an addition of 0.5 wt% Al-5Ti-1B commercial refiner was chosen, in which faceted Pt-rich $\text{Al}_{24}\text{Pt}_9\text{Er}_4$ IMCs formed as the primary phase. The reasons for choosing this composition are:

1. $\text{Al}_{24}\text{Pt}_9\text{Er}_4$ has a triclinic crystal structure with a monoclinic sub-cell [31] that has the same space group (C2/m) as $\text{Al}_{13}\text{Fe}_4$ [32], which is frequently found in engineering Al alloys and deleterious to alloy mechanical properties [28, 29].

2. Pt has a relatively high energy X-ray absorption K-edge of 78 keV. At the beam energy used for this work (described in more detail in the next section), micro-segregation of Pt into the Pt-rich IMCs provided strong absorption contrast between the solid IMCs and the surrounding liquid, facilitating prompt detection of new crystals and solute patterns in the liquid.
3. In the same experiments, the capability of a new type of X-ray spectrometer, known as “HEXITEC” [33–37] was investigated, which allowed separate identification and spatial mapping of each element in a multi-element alloy (as opposed to radiography/tomography that is only suitable for mapping one element in a binary or pseudo-binary alloy). As the current paper is focusing on radiography, detailed description of this multi-element mapping technique is therefore beyond the scope of the paper, but some latest results of multi-solute segregation mapping from these experiments can be found in [38].

2.2 Sample preparation

Al-23Pt-20Er with 0.5 wt% Al-5Ti-1B were prepared following a four-step procedure. First, TiB₂-containing Al was prepared by adding 0.9 wt% Al-5Ti-1B into molten, pure Al (99.999%) at 750°C in an induction furnace, and the melt was cast into a water-cooled Cu mould. The TiB₂-containing Al was remelted and mixed with pure Er (99.9%) and pure Pt (99.95%) using vacuum arc melting. The ingot was flipped in the arc melting crucible and remelted three times to promote mixing. The outcome was a cap-shaped ingot of ~100 g, with ~50 mm diameter and ~15 mm thickness, as shown schematically in Fig. 1. The top surface was ground with SiC paper, and the edges machined to remove any surface oxide films. The ingot was then cut by a water jet into four pieces (as denoted by the yellow dashed lines). Foil samples were produced by sectioning using a diamond wheel blade. Finally, X-ray radiography samples of 20×10 mm and thickness of 200 ± 5 μm were prepared by grinding and polishing to a final surface finish of 1 μm. Each sample was encapsulated in an X-ray transparent BN cell (Multi-lab, UK) of 100 μm thickness.

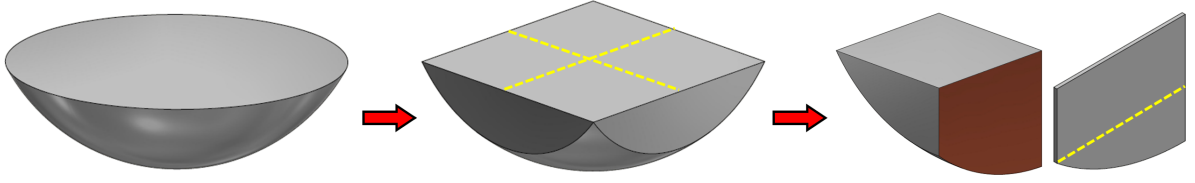


Figure 1: Schematic showing how foil samples were sectioned from a bulk Al-Pt-Er ingot. The as-cast ingot was cut by a water jet as indicated by the yellow dashed lines, and finally sectioned using a diamond wheel blade to produce foil samples.

Electron microscopy was performed on both the as-cast alloy and samples solidified in the synchrotron experiments, for phase identification as a function of solidification conditions. Details can be found in S1 of the supplementary materials.

2.3 Synchrotron X-ray radiography

Synchrotron X-ray radiography experiments were carried out at beamline ID19, European Synchrotron Radiation Facility (ESRF), France, using a bespoke solidification rig that has been described elsewhere [30]. The rig was operated with a controlled Ar atmosphere to protect foil samples and the heating elements from oxidation.

Fig. 2 shows a schematic of the experimental set-up. The sample was illuminated with a pink X-ray beam peaking at 89 keV. The transmitted beam from the sample was collected onto a 200 μm thick LuAG:Ce ($\text{Lu}_3\text{Al}_5\text{O}_{12}:\text{Ce}$) single crystal scintillator, which then projected the radiographic image onto a CMOS PCO.Edge 4.2 camera through an optical system (lenses and mirror). As mentioned earlier, the experiments formed part of a larger experimental campaign of simultaneous radiography and fluorescence imaging. Therefore to allow simultaneous collection of the fluorescence X-ray using the HEXITEC spectrometer, the sample was positioned at 45° to the incident beam. Again, detailed description of the fluorescence imaging is beyond the scope of this paper. Radiography videos were recorded at 10 Hz with an image pixel size of 2.2 $\mu\text{m}/\text{pixel}$ along the vertical direction and an image pixel size of 3.1 $\mu\text{m}/\text{pixel}$ along the horizontal direction, because of the 45° angle between the incident beam and the sample.

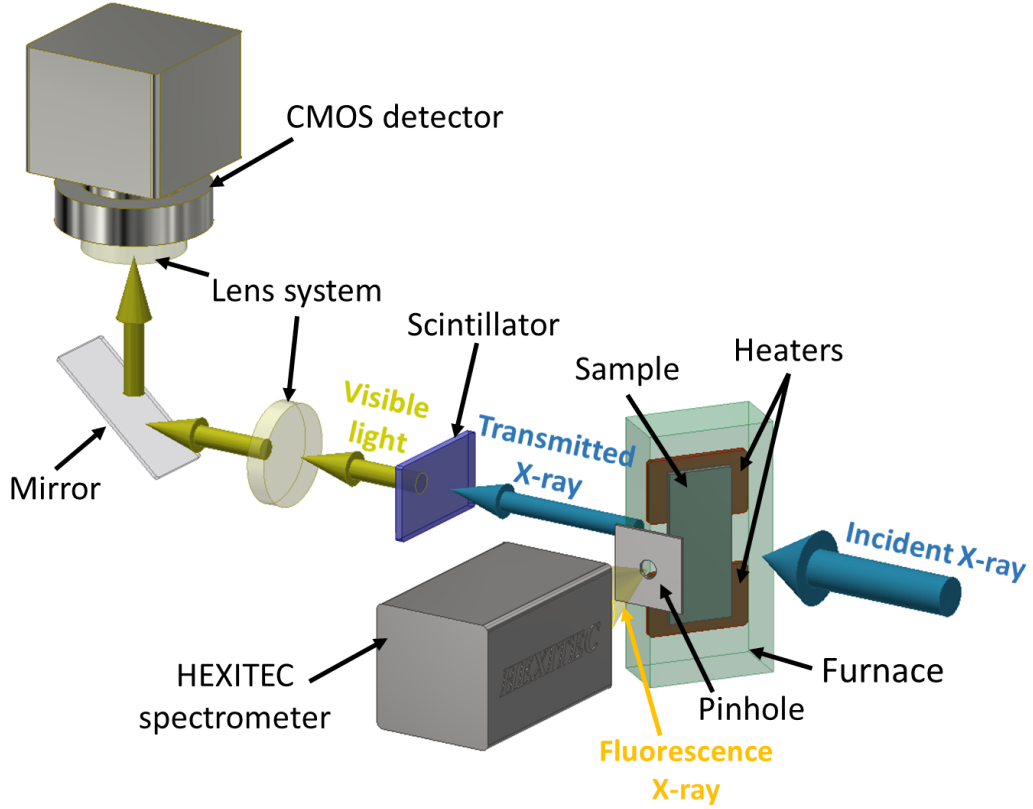


Figure 2: Schematic of the experimental set-up for synchrotron X-ray radiography and simultaneous X-ray fluorescence.

Each sample was fully melted and held at 1200°C for 3 min, then cooled at a constant cooling rate ranging from 0.1 Ks⁻¹ to 8 Ks⁻¹. Table 1 lists all the experimental conditions, together with the number of repeats and the number of IMC crystals measured in each condition. 11 experiments were performed in a directional (bottom-to-top) solidification condition, by maintaining a constant thermal gradient of approximately 15 K mm⁻¹ in the solidifying sample. By carefully calibrating the heater and the furnace, an isothermal solidification sequence was also contrived. Overall, 12 experiments were carried out and the formation of 4,037 IMC particles was detected.

Raw radiographic images acquired were often affected by sample surface imperfections (e.g. scratches) and illumination variations due to defects in the optical system. Therefore, the raw images were processed following a procedure described in S2 of the supplementary materials.

Alloy	Thermal gradient (K mm^{-1})	Cooling rate (K s^{-1})					
		0.1	0.5	1	2	4	8
AlPtEr + TiB_2	15	1 (83)	2 (509)	3 (1002)	2 (712)	2 (824)	1 (458)
AlPtEr + TiB_2	0					1 (449)	

Table 1: Summary of experimental conditions, showing the number of repeats and the number of IMC crystals measured (in parenthesis) in each condition.

3 Results

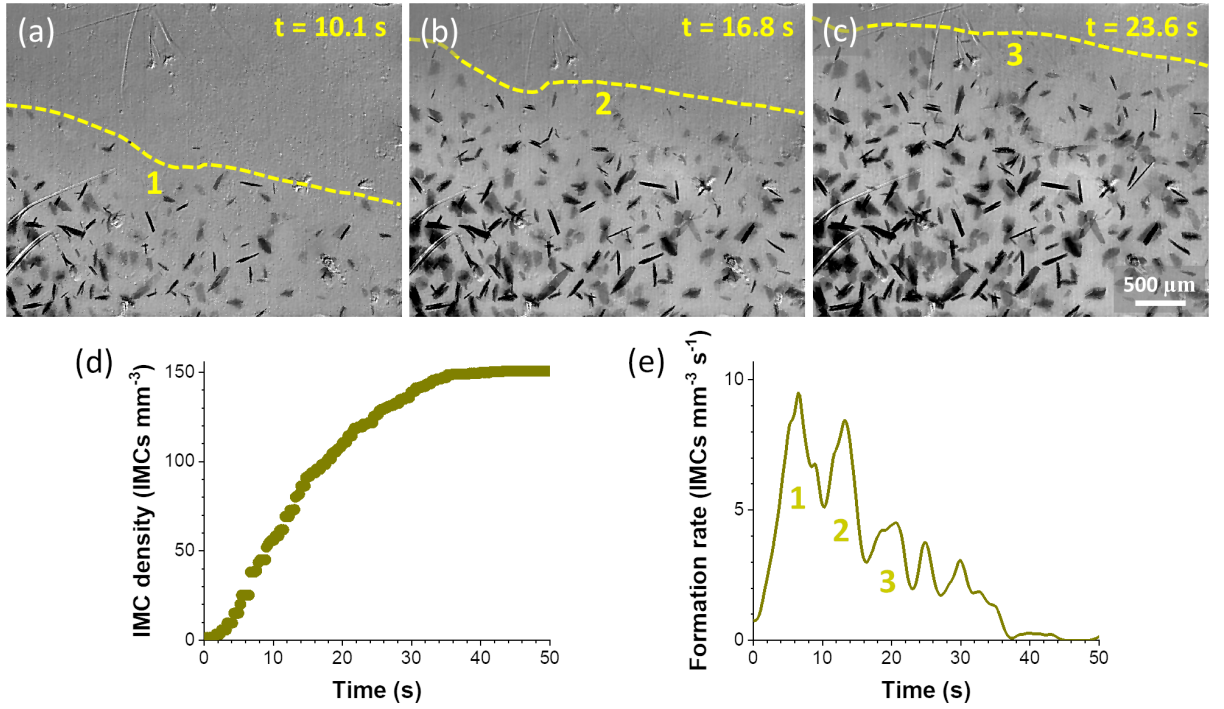


Figure 3: (a) to (c) An example radiograph sequence showing the formation of primary IMC crystals in the solidifying Al-Pt-Er alloy at 2 K s^{-1} and 15 K mm^{-1} . The image field of view is approximately $4 \text{ mm} \times 3 \text{ mm}$. Time $t = 0$ was set when an IMC crystal first appeared in the field of view. IMC formation occurred in 3 waves, denoted as “1”, “2” and “3” in the radiographs, and the yellow dashed line highlights the front of each formation wave. (d) The number density of the IMC formation events in the field of view as a function of time. (e) The IMC formation rate as a function of time. The 3 major waves in (e) were labelled, in correspondence to the formation waves shown in (a) to (c).

Figs. 3(a) to (c) show a radiographic image sequence of the alloy solidifying at 2 K s^{-1} and 15 K mm^{-1} . Time $t = 0$ was set when an IMC crystal first appeared in the field of view. Because of the thermal gradient imposed, the formation of the primary Pt-rich IMCs started near the bottom of the field of view and proceeded upwards. The IMC crystals formed in 3 distinct waves (denoted as 1, 2 and 3 in Figs. 3(a) to

(c)), and a yellow dashed line is superimposed on each frame to highlight the front of each formation wave. Readers are invited to watch the radiographic video (Video 1) in the on-line supplementary materials. Fig. 3(d) shows the number of IMC formation events in the radiographic field of view as a function of time. The vast majority (95%) of the IMC crystals formed in the first 33 seconds. Overall, 390 IMC crystals formed in the field of view by the end of the solidification sequence. The time-resolved formation rate (Fig. 3(e)), by spline interpolating and differentiating the number of formation events, occurred primarily in 3 cascades, corresponding to the formation waves in Figs. 3(a) to (c). Crystal formation waves have only been previously reported for disordered, non-faceted solid solution phases, such as primary equiaxed α -Al dendrites under isothermal and gradient conditions [24–26], whereas the current work is the first of ordered, faceted IMC formation waves.

Figs. 4(a) to (d) present radiographs at the end of the primary IMC formation for different cooling rates, at 15 K mm^{-1} . IMCs at higher cooling rates were noticeably finer and more populous compared with those at 0.5 K s^{-1} . In each case, crystals near the bottom of the field of view were larger and thicker (more X-ray absorbing) due to more time for growth/coarsening, which was more significant at lower cooling rates (Figs. 4(a) and (b)). Overall, 251 primary IMCs formed in the field of view at 0.5 K s^{-1} , 371 at 1 K s^{-1} , 390 at 2 K s^{-1} , and 405 at 4 K s^{-1} .

Fig. 4(e) shows the time-resolved IMC formation rate for the same experiments shown in Figs. 4(a) to (d). At the lowest cooling rate of 0.5 K s^{-1} , there was no noticeable peak (indicative of a wave or burst of nucleation) in the formation rate profile, and the maximum instantaneous formation rate was approximately $2 \text{ IMCs mm}^{-3} \text{ s}^{-1}$. Formation rate at an intermediate cooling rate of 1 K s^{-1} showed a peak around $t = 20 \text{ s}$ and a peak formation rate of $5 \text{ IMCs mm}^{-3} \text{ s}^{-1}$, with formation then more sluggish. In contrast, the formation rate profiles at 2 K s^{-1} and 4 K s^{-1} showed distinct multiple peaks of $9 \text{ IMCs mm}^{-3} \text{ s}^{-1}$ and $13 \text{ IMCs mm}^{-3} \text{ s}^{-1}$, respectively.

Figs. 5(a) to (c) show a radiograph sequence for directional solidification at 4 K s^{-1} and 15 K mm^{-1} , where the IMC formation started from the bottom of the field of view, proceeded progressively upwards in two distinct waves, and finished

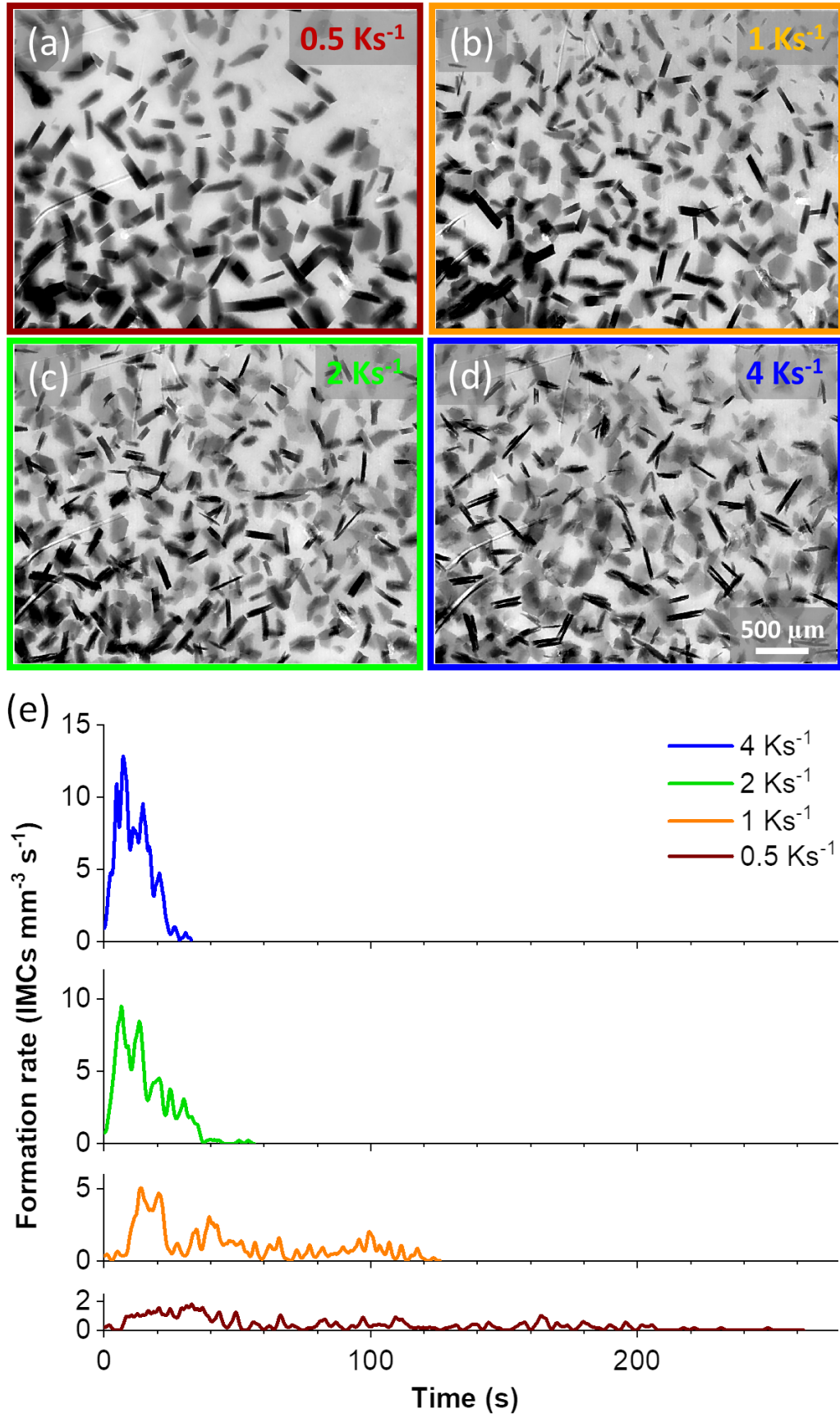


Figure 4: Radiographs at the end of the formation of primary IMCs at (a) 0.5 Ks⁻¹ (b) 1 Ks⁻¹, (c) 2 Ks⁻¹ and (d) 4 Ks⁻¹, at 15 K mm⁻¹. (e) Time resolved IMC formation rate for the experiments shown in (a) to (d).

at ~ 20 s. Figs. 5(d) to (f) show a radiograph sequence at the same cooling rate of 4 K s^{-1} but for the case of isothermal solidification. Now, almost all IMC crystals formed uniformly across the field of view, in a single intense burst in the first 10 s (Fig. 5(e)).

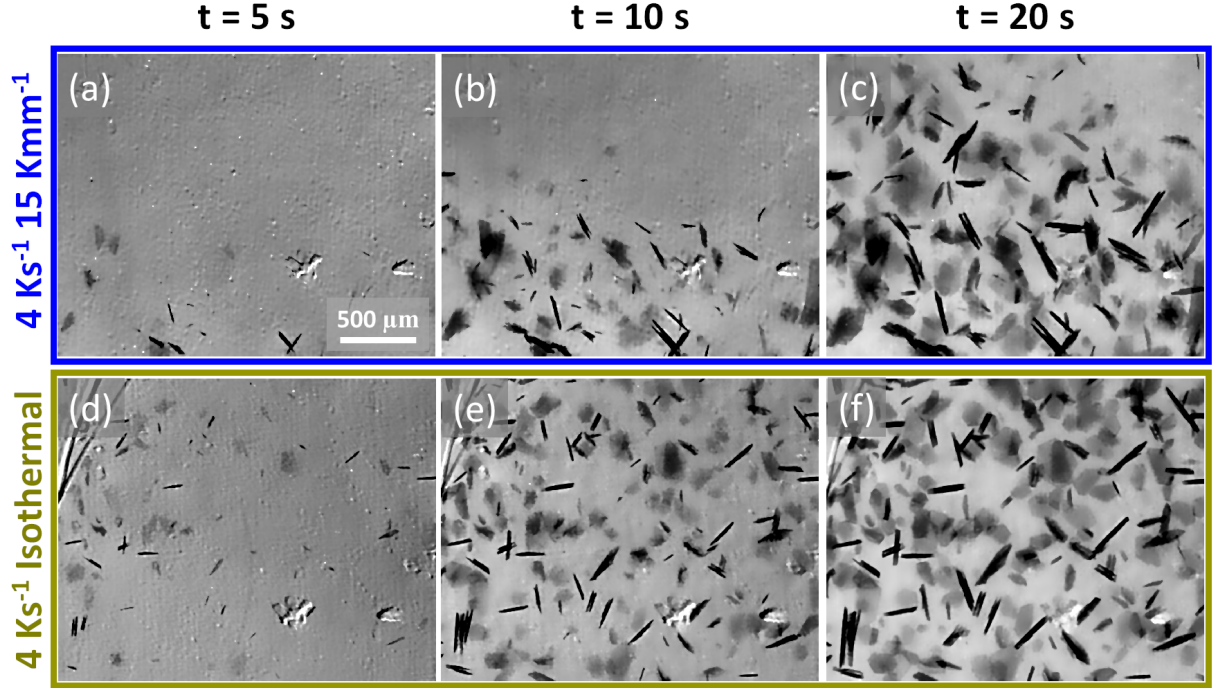


Figure 5: (a) to (c) A radiograph sequence showing the formation of primary IMC crystals at 4 K s^{-1} and 15 K mm^{-1} . (d) to (f) A radiograph sequence showing the formation of primary IMC crystals at 4 K s^{-1} under isothermal cooling conditions.

Fig. 6 shows the time-resolved IMC formation rate for the directional and isothermal sequences in Fig. 5, with peak IMC formation rates of $16 \text{ IMCs mm}^{-3} \text{ s}^{-1}$ and $32 \text{ IMCs mm}^{-3} \text{ s}^{-1}$, respectively. The duration of the IMC formation, here defined as the time for 95% (number fraction) of the IMCs to form, was 10.8 s under the isothermal condition, corresponding to a temperature change of 43 K, and 19.5 s for the directional counterpart, corresponding to a temperature change of 78 K. In total, 152 IMCs formed in the field of view under directional cooling (Figs. 5(a) to (c)), and 183 IMCs formed under isothermal cooling (Figs. 5(d) to (f)). To the best of the authors' knowledge, the effects of a thermal gradient on crystal nucleation bursts have not been studied previously.

Figs. 7(a) and (b) summarise the total IMC number density and the correspond-

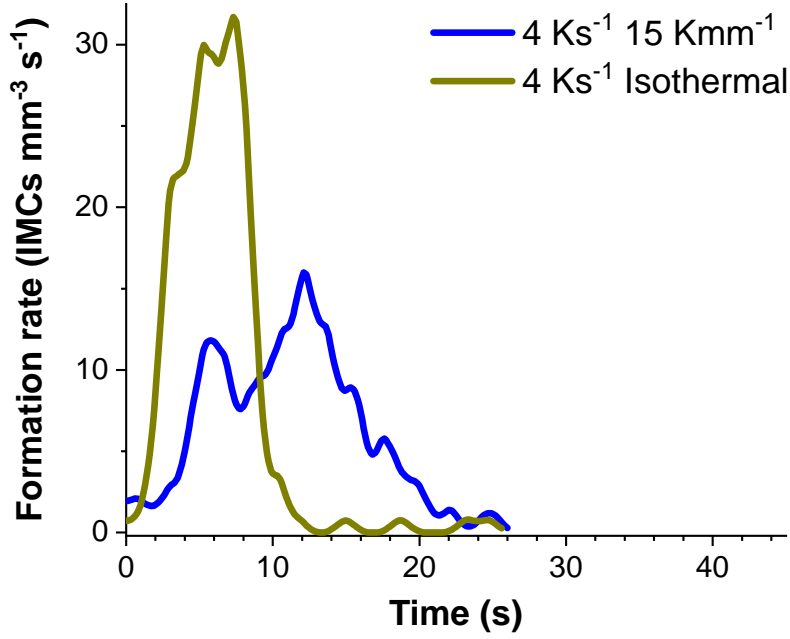


Figure 6: Time resolved IMC formation rate for the directional and isothermal solidification sequences at 4 Ks^{-1} shown in Fig. 5.

ing average formation rate in the 11 directional solidification experiments (shown by the purple dots) and 1 isothermal experiment (shown by the purple circle). Isothermal solidification showed the highest IMC number density of 197 IMCs mm^{-3} . The number density under directional conditions first increased rapidly with cooling rate, from 21 IMCs mm^{-3} at 0.1 Ks^{-1} to $99 \pm 3 \text{ IMCs mm}^{-3}$ at 0.5 Ks^{-1} . However, it then became less sensitive to the cooling rate, increasing to $125 \pm 20 \text{ IMCs mm}^{-3}$ at 1 Ks^{-1} , and levelled off at approximately 150 IMCs mm^{-3} with further increases in cooling rate up to 8 Ks^{-1} . Similarly, a weak relationship between the IMC number density and cooling rate was reported for primary $\text{Al}_{13}\text{Fe}_4$ during directional solidification of an Al-5Ti-1B inoculated Al-3Fe (wt%) at 5 K mm^{-1} and 8 K mm^{-1} in the cooling rate range 0.5 Ks^{-1} to 4 Ks^{-1} [30], and these data are also plotted in Fig. 7(a) for comparison. The number density of $\text{Al}_{13}\text{Fe}_4$ IMCs fluctuated between 50 and 75 IMCs mm^{-3} at 5 K mm^{-1} (solid gold diamonds in Fig. 7(a)), and levelled off at approximately 20 IMCs mm^{-3} for a higher thermal gradient of 8 K mm^{-1} (hollow gold diamonds in Fig. 7(a)). Comparing the trend-wise effect of the cooling rate on

the Pt-rich and the Fe-rich IMC number density, both showed a weak sensitivity at cooling rate $\dot{T} > 0.5 \text{ K s}^{-1}$, whilst at $\dot{T} = 0.1 \text{ K s}^{-1}$ to $\dot{T} = 0.5 \text{ K s}^{-1}$ (where data is available for the Pt-rich IMCs) the number density of Pt-rich IMCs showed a rapid increase.

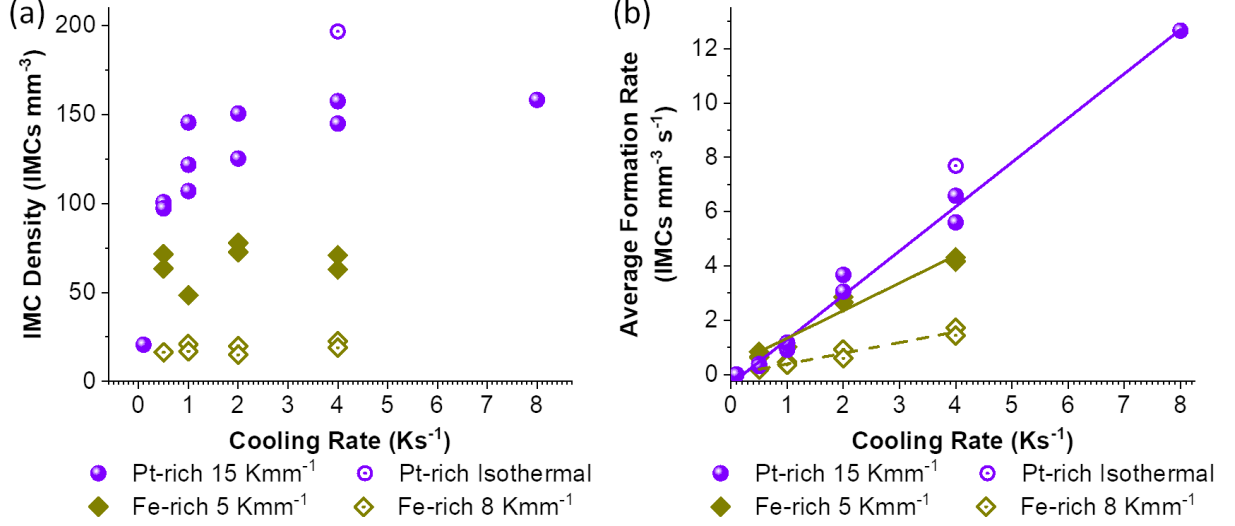


Figure 7: (a) Total IMC number density for 11 directional solidification experiments at 15 K mm^{-1} (shown by the purple dots) and 1 isothermal experiment (shown by the purple circle). The solid and hollow gold diamonds denote the IMC density of $\text{Al}_{13}\text{Fe}_4$ at 5 K mm^{-1} and 8 K mm^{-1} , respectively, taken from [30]. (b) Average IMC formation rate for 11 directional solidification experiments at 15 K mm^{-1} (shown by the purple dots) and 1 isothermal experiment (shown by the purple circle). The purple line indicates a linear best-fit to highlight the trend of the formation rate for directional solidification (quality of fitting: $R^2 = 0.992$). The solid and hollow gold diamonds denote the average formation rate of $\text{Al}_{13}\text{Fe}_4$ at 5 K mm^{-1} and 8 K mm^{-1} , respectively, taken from [30].

The average formation rate of the Pt-rich IMCs in the directional conditions (shown by the purple dots in Fig. 7(b)) followed a linear trend, increasing from $0.005 \text{ IMCs mm}^{-3}\text{s}^{-1}$ at 0.1 K s^{-1} to $13 \text{ IMCs mm}^{-3}\text{s}^{-1}$ at 8 K s^{-1} . Similarly, there was a linear trend for the average formation rate of primary $\text{Al}_{13}\text{Fe}_4$ [30]. The average formation rate of the Pt-rich IMCs in the isothermal condition (approximately $8 \text{ IMCs mm}^{-3}\text{s}^{-1}$) was noticeably higher than the directional counterpart ($6 \pm 0.5 \text{ IMCs mm}^{-3}\text{s}^{-1}$) for the same cooling rate.

4 Discussion

4.1 Nucleants

The number density of Pt-rich IMCs showed a rapid increase from 0.1 Ks^{-1} to 0.5 Ks^{-1} , but a weak relationship at higher cooling rates, and had a similar trend to Fe-rich IMCs for $\dot{T} > 0.5 \text{ Ks}^{-1}$ (Fig. 7(a)). This suggests that for a given type of IMC to be formed, a similar population of nucleants suitable for IMC formation were activated, regardless of cooling rate. In other words, increasing the cooling rate over the range studied did not activate a significantly different number of effective nucleant particles in the melt.

Fig. S1(d) in the supplementary materials shows a TiB_2 particle sitting inside a Pt-rich IMC crystal, suggesting that TiB_2 acted as a nucleant. According to the free growth model for heterogeneous nucleation [9, 39], larger TiB_2 particles have a lower energy barrier (i.e. a higher potency) for the nucleation of solid crystals. The size distribution of the TiB_2 particles in commercial Al-5Ti-1B is approximated as a log-normal distribution [40, 41] in the form of:

$$N(d) = \frac{N_0}{\sigma d \sqrt{2\pi}} \exp\left(-\frac{[\ln(d) - \ln(d_0)]^2}{2\sigma^2}\right) \quad (1)$$

where $N(d)$ is the number density of the TiB_2 particles of a diameter d , N_0 is the total number density of TiB_2 particles, $d_0 = 0.68 \text{ }\mu\text{m}$ is the geometric mean diameter, and $\sigma = 0.876$ is the geometric standard deviation [41]. For a 0.1 wt% addition of Al-5Ti-1B in [41], the total number density of TiB_2 particles was $N_0 = 7.3 \times 10^3 \text{ mm}^{-3}$. Therefore, for 0.5 wt% addition of Al-5Ti-1B used in the current work, the total TiB_2 number density was assumed to be approximately $N_0 = 3.65 \times 10^4 \text{ mm}^{-3}$.

By integration of Eq. 1, the number density of the most potent TiB_2 particles, assumed to be those with diameter $>6 \text{ }\mu\text{m}$, was estimated to be approximately 200 mm^{-3} , accounting for $\sim 0.5\%$ of the total TiB_2 number density in the melt. Potent oxide particles in the melt and the oxide skin of the foil can also catalyse

IMC formation particularly when there are no extrinsic inoculants available [42–47]. The estimated number density of the most potent nucleant particles was thus relatively close to the maximum number density of Pt-rich IMCs of 160 mm^{-3} under directional solidification and 197 mm^{-3} under isothermal solidification. Therefore, taking this semi-quantified comparison, microstructural evidence and previous work [30, 48, 49], it is not unreasonable to assume that IMC crystals nucleated predominantly on larger TiB_2 particles. Of course, all the TiB_2 - and other extrinsic particulates - have the potential to catalyse the formation of an IMC; the extent to which they are in practice activated or remain dormant depends on the local undercooling conditions in the liquid in which they sit, i.e. the available undercooling in the liquid.

4.2 Available undercooling in the liquid

As shown in S1 in the supplementary materials, the Pt-rich IMCs had the same Er concentration as the bulk alloy. Er was added to the alloy only to facilitate the simultaneous multi-element fluorescence mapping study [38], and for the purpose of the current paper, the Er segregation effect on IMC formation can be ignored, and the alloy can be treated as a pseudo binary system.

Following the procedure described in S2.2 in the supplementary materials, Fig. 8(a) shows the micro-segregation of Pt, expressed as $\mu \Delta C$, measured in the liquid ahead of a typical growing IMC, along the direction indicated by the black arrow in the inset radiograph of the Pt diffusion field. ΔC is the difference between the local Pt concentration (i.e. at any point along the direction) and the bulk Pt concentration, and μ is the X-ray mass attenuation coefficient of Pt. Pt was depleted at the solid/liquid interface ($x = 0$) as it segregated preferentially into the IMC, and relative concentration increased gradually towards the bulk, far-field Pt concentration (Fig. 8(a)). The red curve in Fig. 8(a) indicates a best-fit of the equation $y = a + b e^{-cx}$ to the concentration profile according to the theory of micro-segregation [50], with $R^2 = 0.994$ indicating an excellent fit.

The magnitude of the available undercooling ΔT in the liquid (also named the

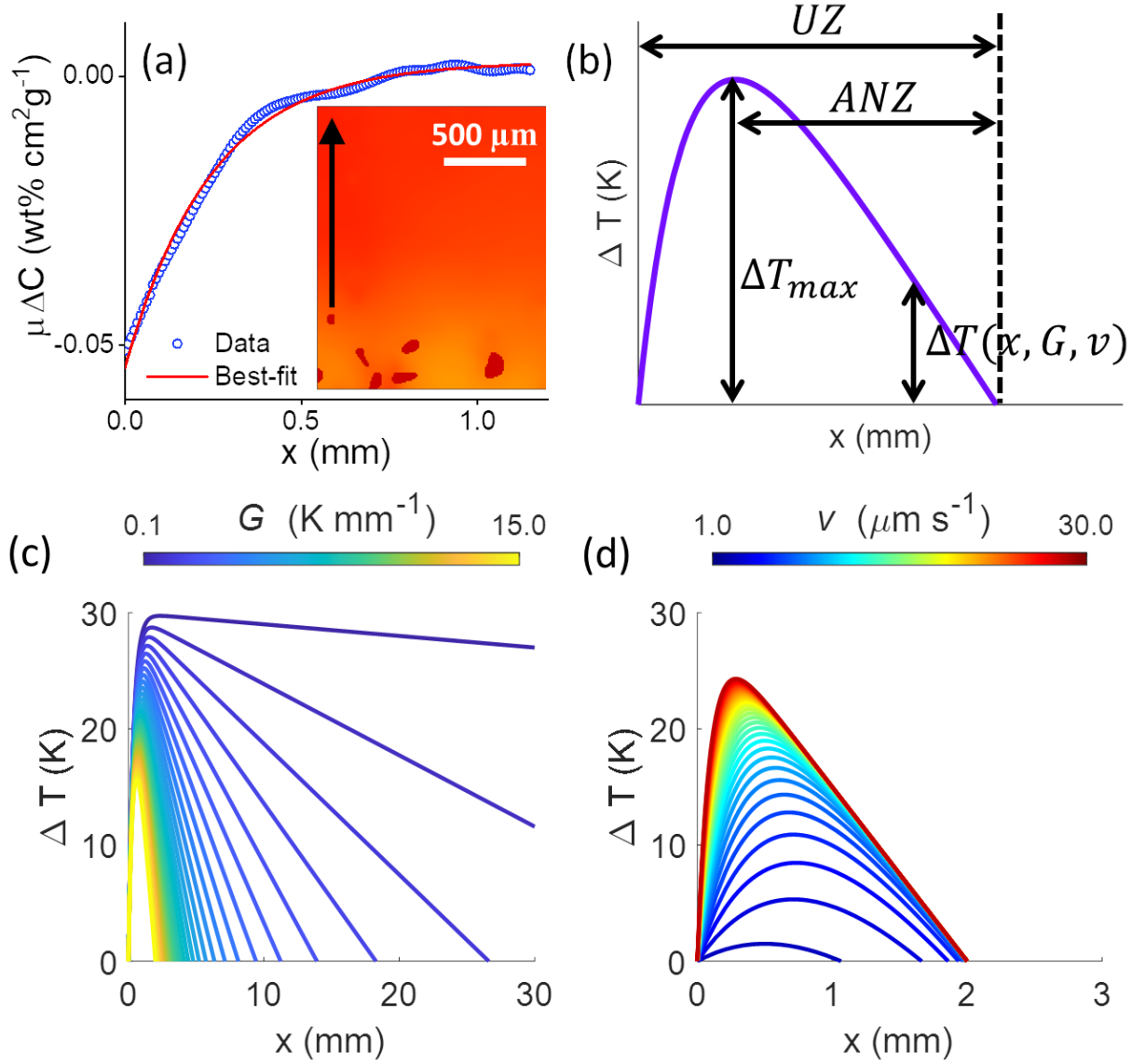


Figure 8: (a) The micro-segregation of Pt, expressed as $\mu\Delta C$, ahead of a typical growing IMC along the direction indicated by the black arrow in the inset radiograph of the Pt diffusion field, with a best-fit to equation $y = a + be^{-cx}$ ($R^2 = 0.994$). μ is the X-ray mass attenuation coefficient of Pt (constant), and ΔC is the difference between the local Pt concentration ahead of a growing IMC and the bulk Pt concentration. (b) A schematic of the available undercooling ΔT in the liquid in front of a growing IMC crystal at a thermal gradient G and a growth velocity v . (c) ΔT as a function of x calculated from Eq. 2 at thermal gradients G between 0.1 K mm^{-1} and 15 K mm^{-1} for a growth velocity of $v = 8 \mu\text{m s}^{-1}$. (d) ΔT as a function of x for growth velocities between $1 \mu\text{m s}^{-1}$ and $30 \mu\text{m s}^{-1}$ at a thermal gradient of 15 K mm^{-1} . The following parameters were used for the calculation of (c) and (d): $\Delta C_0 = -1 \text{ wt\%}$, $m = 30 \text{ K wt\%}^{-1}$, $D_l = 3 \times 10^{-9} \text{ m}^2\text{s}^{-1}$.

“constitutional supercooling” in the interdependence model [11]), arising from the micro-segregation (depletion) of Pt in front of a growing Pt-rich IMC crystal, is

given by [30]:

$$\Delta T(x, G, v) = m\Delta C_0(e^{-x\frac{v}{D_l}} - 1) - xG \quad (2)$$

where m is the slope of the liquidus, ΔC_0 is the composition difference between the bulk liquid and the liquid at the solid/liquid interface, D_l is the Pt diffusion coefficient in the liquid, v is the growth velocity of the interface, G is the thermal gradient and x is the distance from the interface.

Fig. 8(b) presents a schematic depiction of the available undercooling ΔT as a function of the distance x at a thermal gradient G and a growth velocity v . UZ denotes the extent of the undercooled zone. As directional cooling proceeds, the UZ translates progressively along positive x , and at any instant, nucleant particles that first experienced $\Delta T(x, G, v) > \Delta T_n$, where ΔT_n is the undercooling required for nucleation on a given nucleant particle and a function of particle size, become activated for IMC nucleation. Hence for any instant shown in Fig. 8(b), new IMC formation events only occur in the advancing region of the UZ (i.e the region to the right of ΔT_{max}), here termed the “active nucleation zone” (ANZ) [51]. This is because any potent particle to the left of ΔT_{max} will have already been activated as the UZ develops.

Fig. 8(c) shows ΔT as a function of the distance x calculated from Eq. 2 at a range of thermal gradients G between 0.1 K mm^{-1} and 15 K mm^{-1} , for a growth velocity of $v = 8 \text{ } \mu\text{m s}^{-1}$. Increasing the thermal gradient G had a strong effect on reducing both the extent of UZ and the magnitude of ΔT . Fig. 8(d) shows ΔT as a function of x at a range of growth velocities between $1 \text{ } \mu\text{m s}^{-1}$ and $30 \text{ } \mu\text{m s}^{-1}$ representative of measured IMC growth velocities from the radiographic sequences, for a thermal gradient of 15 K mm^{-1} . Increasing the growth velocity v initially strongly increased ΔT ($v < 10 \text{ } \mu\text{m s}^{-1}$), but ΔT became less sensitive to further increases in growth velocity. The size of UZ was almost insensitive to growth velocity for $v > 3 \text{ } \mu\text{m s}^{-1}$, but there was a shift in the point of maximum undercooling towards the IMC/liquid interface, indicating an extension in ANZ . The size of the undercooled

zone $UZ(G, v)$ is given by [30]:

$$UZ(G, v) = -\frac{1}{G} \left[\Delta C_0 m - \frac{D_l}{v} G W_0 \left(\frac{\Delta C_0 m}{G} \frac{v}{D_l} e^{\frac{\Delta C_0 m}{G} \frac{v}{D_l}} \right) \right] \quad (3)$$

where W_0 is the principal branch of the Lambert W function [52]. Correspondingly,
 315 the size of the active nucleation zone $ANZ(G, v)$, i.e. the distance between the
 advancing boundary of the UZ and the peak position is:

$$ANZ(G, v) = -\frac{1}{G} \left[\Delta C_0 m - \frac{D_l}{v} G W_0 \left(\frac{\Delta C_0 m}{G} \frac{v}{D_l} e^{\frac{\Delta C_0 m}{G} \frac{v}{D_l}} \right) \right] + \frac{D_l}{v} \ln \left(-\frac{G D_l}{m \Delta C_0 v} \right) \quad (4)$$

The maximum available undercooling $\Delta T_{max}(G, v)$ is given by:

$$\Delta T_{max}(G, v) = G \frac{D_l}{v} \left[\ln \left(-\frac{G}{m \Delta C_0} \frac{D_l}{v} \right) - 1 \right] - m \Delta C_0 \quad (5)$$

Fig. 9 (a) shows the size of $ANZ(G, v)$ as a function of growth velocity (which is in
 turn related to cooling rate) for a range of thermal gradients between 0.1 K mm^{-1}
 320 and 15 K mm^{-1} . At each thermal gradient G in Fig. 9 (a), the ANZ first increased
 at smaller growth velocity and then levelled off despite further increases. For ex-
 ample, at $G = 15 \text{ K mm}^{-1}$ (as shown in a more detailed view in the inset graph of
 Fig. 9 (a)) the ANZ increased from approximately 0.5 mm to 1.3 mm as the growth
 velocity increased from $2 \mu\text{m s}^{-1}$ to $8 \mu\text{m s}^{-1}$. It then extended only slightly from
 325 1.3 mm to 1.5 mm as the velocity increased to $13 \mu\text{m s}^{-1}$; there was no significant
 further increase so that $ANZ = 1.6 \text{ mm}$ at $v = 20 \mu\text{m s}^{-1}$ and $ANZ = 1.7 \text{ mm}$ at
 $v = 30 \mu\text{m s}^{-1}$.

ΔT_{max} at a given thermal gradient G in Fig. 9 (b) showed a similar trend.
 For $G = 15 \text{ K mm}^{-1}$, ΔT_{max} first increased rapidly from 2 K at $2 \mu\text{m s}^{-1}$ to 16 K at
 330 $8 \mu\text{m s}^{-1}$. The curve then flattened, giving $\Delta T_{max} = 20 \text{ K}$ at $13 \mu\text{m s}^{-1}$, $\Delta T_{max} = 22$
 K at $20 \mu\text{m s}^{-1}$ and $\Delta T_{max} = 24 \text{ K}$ at $30 \mu\text{m s}^{-1}$.

Taking these trends together shows that isothermal cooling provided the largest

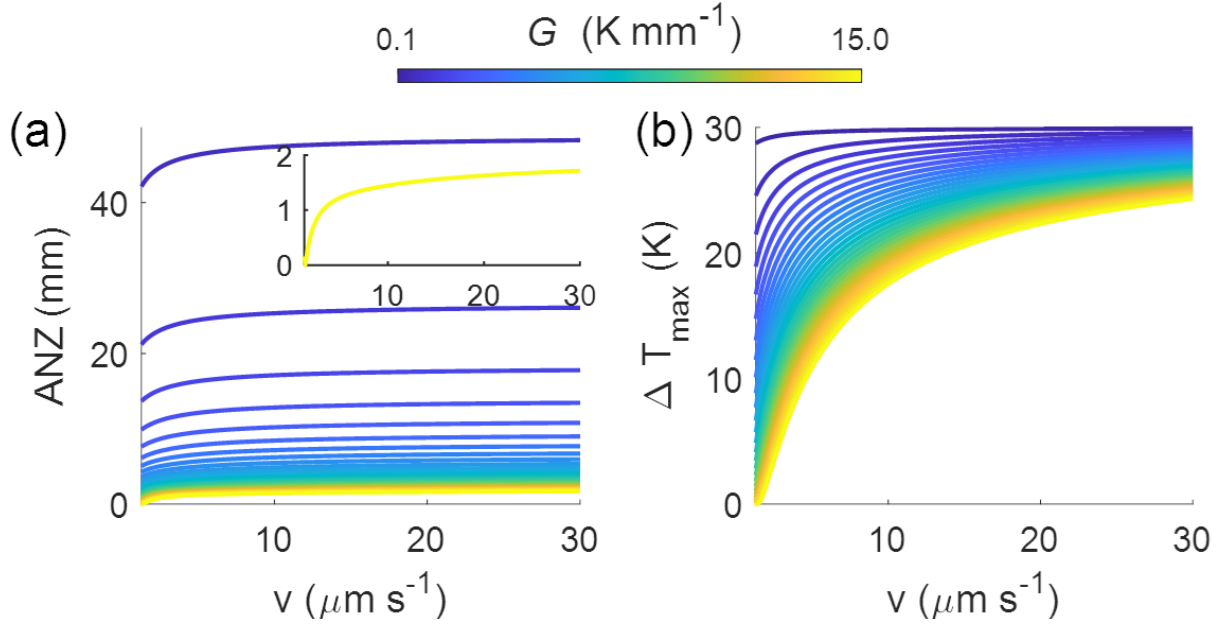


Figure 9: (a) ANZ as a function of growth velocity for thermal gradients between 0.1 K mm^{-1} and 15 K mm^{-1} . The inset graph presents a more detailed view for $G = 15 \text{ K mm}^{-1}$. (b) ΔT_{max} as a function of growth velocity for thermal gradients between 0.1 K mm^{-1} and 15 K mm^{-1} . The following parameters were used: $\Delta C_0 = -1 \text{ wt\%}$, $m = 30 \text{ K wt\%}^{-1}$, $D_l = 3 \times 10^{-9} \text{ m}^2 \text{ s}^{-1}$.

ANZ , and that where a thermal gradient G was present, it had a dominant effect on the size of ANZ (Fig. 9(a)). Under isothermal cooling, all the most potent nucleants in the melt became active to catalyse IMC nucleation, almost simultaneously and in the form of an intense single burst or wave (Fig. 6). Under a thermal gradient $G = 15 \text{ K mm}^{-1}$, both ANZ and ΔT_{max} increased at small v (Figs. 9(a) and (b)), which explains the higher IMC number density as cooling rate increased from 0.1 K s^{-1} to 0.5 K s^{-1} (purple dots in Fig. 7(a)). However, as ANZ and ΔT_{max} stabilised at increasing v (i.e. as the cooling rate increased), the IMC number density correspondingly showed a weakened sensitivity to cooling rate (Fig. 7(a)).

4.3 Solute suppression

The last section focused on the solute diffusion field and the resultant available undercooling at a given time instant in front of an individual solid/liquid interface. In this section, the hypothesis, based on experiments, that nucleation bursts promoted a better efficiency for IMC formation than quasi-continuous nucleation is explored by considering the way in which solute was distributed across the field of view, in

terms of the competition between formation of new IMCs, and the growth or coarsening of existing IMCs. The key difference is that here, and consistent with the concept of the interdependence model [11], we now consider an ensemble of IMC crystals rather than consideration of a single IMC in liquid, isolated from its neighbours. As we show by experiment, IMCs are far from isolated from one another in terms of their associated solute fields.

Following the procedure of image processing detailed in S2.2 in the supplementary materials, Figs. 10(a) to (c) present three contour map sequences showing the fraction of Pt-depleted liquid (f_{dep}) for directional solidification conditions at 0.5 Ks^{-1} and 4 Ks^{-1} , and for isothermal solidification conditions at 4 Ks^{-1} , respectively. The maps top to bottom are at different temperatures related to T_0 , where T_0 is the temperature when an IMC crystal first appeared in the field of view in each sequence. The Pt-depleted liquid was defined as pixels in the liquid where the greyscale intensity change $\Delta P > \Delta P^* = 0.03$, and is coloured yellow in each image. The relatively weak influence of changing the ΔP^* assumption is evaluated in Fig. S4 in the supplementary materials, and confirms that the assumed value of ΔP^* does not affect the trend-wise insights described below.

In each sequence, f_{dep} increased as solidification proceeded, as can be expected as primary Pt-rich IMCs continued to form and/or coarsen, consuming Pt from the liquid. At each temperature ($T_0 - T$), the alloy solidified directionally at 0.5 Ks^{-1} had the largest liquid fraction depleted, which decreased as the cooling rate increased to 4 Ks^{-1} for the same thermal gradient. A similar observation of a shrinking solute affected zone was reported by Jia *et al.* during the directional solidification of an equiaxed Al-15wt%Cu at cooling rates of 0.1 Ks^{-1} to 1 Ks^{-1} [25]. In comparison with the two directional solidification sequences in Figs. 10(a) and (b), the isothermal sequence in Fig. 10(c) showed the smallest liquid fraction depleted at each $T_0 - T$.

Fig. 10(d) replots the time-resolved IMC formation rate as a function of $(T_0 - T)$. There was a relatively narrow, intense peak for the isothermal cooling, two less pronounced peaks spread over a wider range of temperature interval for 4 Ks^{-1} and

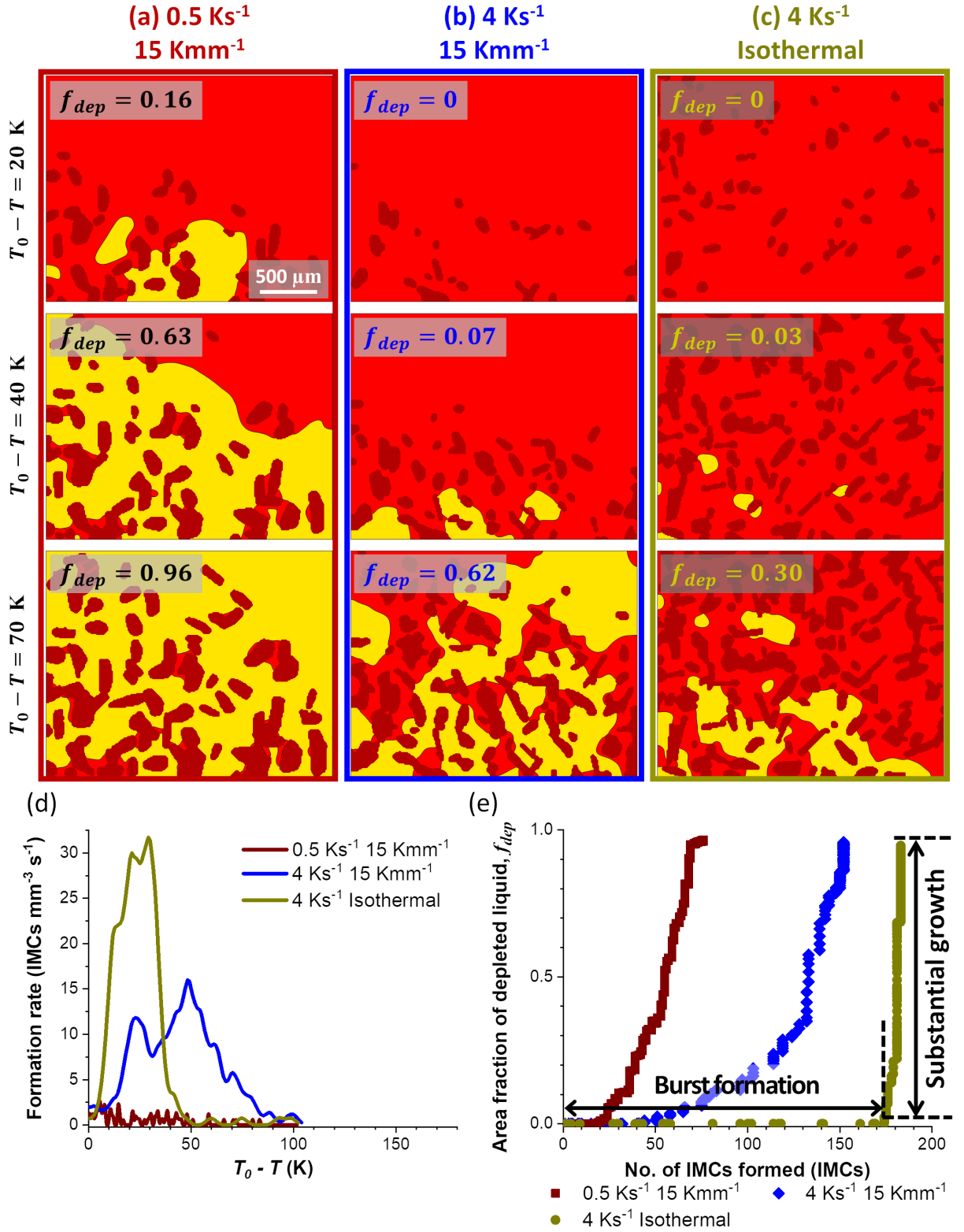


Figure 10: Contour map sequences showing the area fraction of Pt-depleted liquid (f_{dep}) during IMC formation at (a) 0.5 Ks^{-1} and (b) 4 Ks^{-1} during directional solidification and at (c) 4 Ks^{-1} for isothermal solidification, respectively. T_0 is the temperature when an IMC crystal first appeared in the field of view. As described in S2.2 in the supplementary materials, each image was obtained by subtracting the current frame with a reference frame of a flat intensity field acquired before solidification started. The Pt-depleted liquid was defined as pixels in the liquid where the greyscale intensity change $\Delta P > \Delta P^* = 0.03$, and is coloured yellow in each image. (d) Time-resolved IMC formation rate as a function of $(T_0 - T)$. (e) The liquid fraction depleted as a function of the number of IMCs formed in the field of view.

15 K mm⁻¹, and no distinct peaks at 0.5 Ks⁻¹ and 15 K mm⁻¹.

Fig. 10(e) consolidates (a) to (d) using a plot of the liquid fraction depleted (f_{dep}) as a function of the number of IMCs formed in the field of view. A steeper slope in the plot for a given number of IMCs indicates a more rapid increase in the liquid fraction depleted, i.e. the growth of existing IMC crystals dominates the formation of new IMC crystals, because the solute is being depleted from the liquid by existing IMCs. For directional solidification at 0.5 Ks⁻¹, liquid rapidly depleted when only ~20 IMCs had formed (out of 76 IMCs in total, 26%), i.e. there was substantial growth of existing crystals that formed early during cooling. Under directional solidification at 4 Ks⁻¹, there was a more progressive solute depletion of the liquid with progressive formation of IMCs, consistent with Fig. 10(d). Only once ~88% of the total number of IMCs had formed in the field of view, did growth/coarsening begin to dominate. When solidified isothermally at the same cooling rate, there was no solute depletion until practically all (95%) the IMCs appeared in a burst, creating the largest number of IMCs overall and rapidly disrupting the Pt distribution in the liquid (Fig. 10(c)).

Linking back to Fig. 9 in section 4.2, directional solidification at low cooling rate of 0.5 Ks⁻¹ provided a relatively small ANZ and ΔT_{max} , and activated fewer potent nucleants, so the growth of existing crystals and rapid solute depletion was preferred. At 4 Ks⁻¹ and particularly under isothermal solidification, ANZ and ΔT_{max} increased, more nucleants were activated and IMC growth was suppressed in favour of IMC formation.

Fig. 11 presents schematics to illustrate qualitatively the effect of solute field interaction on the number of nucleation events at each time instant for directional (Figs. 11(a) to (d)) and ideally isothermal solidification (Figs. 11(e) to (h)). The green area indicates liquid above the alloy equilibrium melting point, the blue area indicates undercooled liquid, blue dots denote potential potent nucleants in non-undercooled liquid, green dots are nucleants activated for IMC nucleation, and red dots are nucleants where the nucleation is suppressed because they sit in solute-depleted liquid indicated by the green discs.

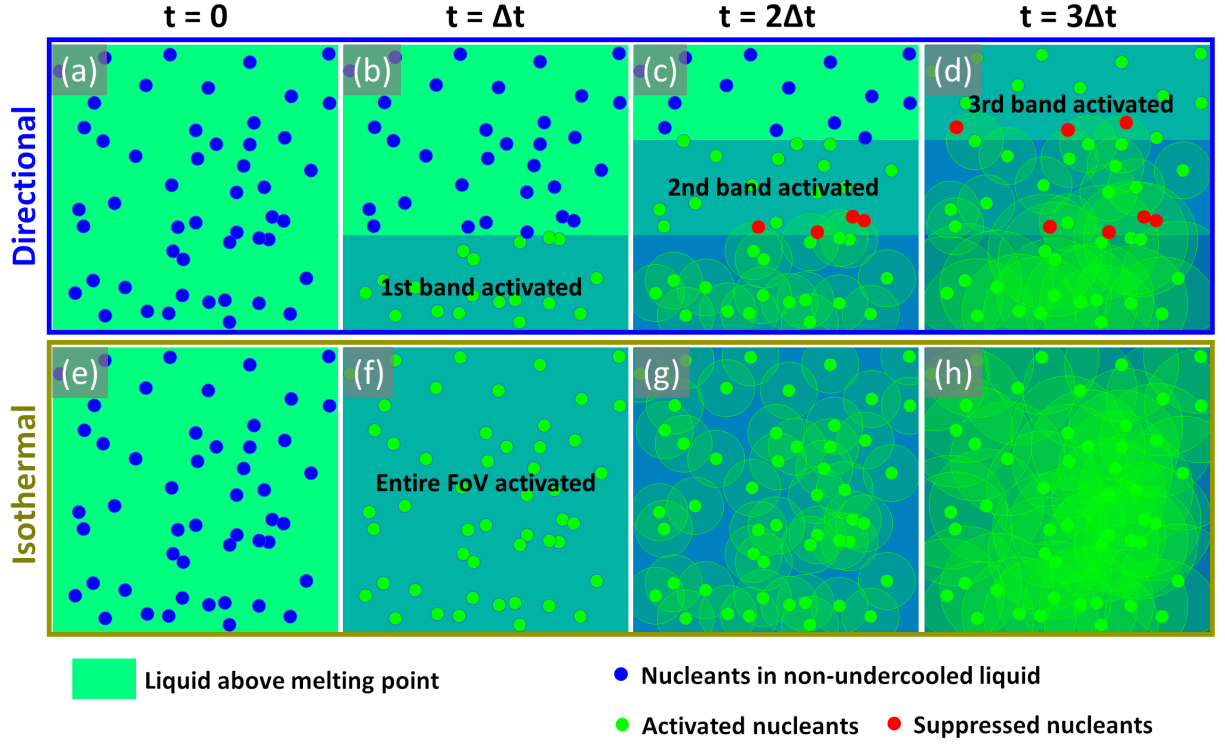


Figure 11: Schematics illustrating the number of activated nucleants at each time instant under (a) to (d) directional, and (e) to (h) ideally isothermal solidification. The green area indicates liquid above the alloy equilibrium melting point, the blue area indicates undercooled liquid, blue dots denote nucleants in non-undercooled liquid, green dots are nucleants activated for IMC nucleation, and red dots are nucleants where the nucleation is suppressed because they sit in solute-depleted liquid indicated by the green discs. The spatial distribution of the nucleant particles was generated as a random array using Matlab.

At time $t = 0$, the liquid is above the alloy melting point, and there are 50 potent nucleants distributed randomly in the field of view. At time $t = \Delta t$, nucleants near the (cooler) bottom are activated under directional cooling (Fig. 11(b)); at the same instant, all nucleants are activated simultaneously under isothermal cooling (Fig. 11(f)). At $t = 2\Delta t$ under directional cooling, the middle band of liquid is undercooled (Fig. 11(c)). However, due to the solute depletion effect caused by the growth of the earlier nucleated crystals in the bottom band, the remaining (red) nucleants in this region are dormant, due to the well-known solute suppressed nucleation effect [10, 26]. At the same instant for isothermal cooling (Fig. 11(g)), there are no new nucleation events, because all the potent nucleants have already been activated. At $t = 3\Delta t$, nucleation occurs in the top band under directional cooling (Fig. 11(d)); only growth/coarsening is possible under isothermal cooling (Fig. 11(h)). Overall, 7 out of 50 (14%) nucleants were suppressed by the solute-

depleted liquid under directional cooling.

In summary, when considering an ensemble of potential nucleants and IMCs, as is the case in castings, it is not only the local solute and undercooling environment at an instant that each nucleant experiences that matters, but also the longer range dynamics of how the nucleants and the solute fields interact. This interaction specifically concerns the development and impingement of the solute fields around each crystal. The results here suggest that the probability of IMC formation at any instant (assuming all nucleants are equally potent) depends on how many IMCs there are already and the fraction of liquid solute depleted, which in turn depends on the macro-scale cooling rate and thermal gradient conditions.

Comparing the solute suppression effect for disordered α -Al in earlier work [24–26], and the ordered IMCs in the current work, there are key differences to be noted. Because of the small nucleation barrier of α -Al on TiB_2 , only relatively low undercoolings are needed even for nucleation on comparatively small TiB_2 particles, for example an undercooling of only ~ 1 K to nucleate on a $0.5\text{ }\mu\text{m}$ TiB_2 , according to the free growth model [9]. This small nucleation undercooling is easily realised by the undercooling available in the liquid. Therefore solute suppression of the larger, very low undercooling but rare TiB_2 particles promotes activation of the more populous, smaller ones, and overall leads to more α -Al crystals [26]. In contrast as discussed in section 4.1, the ordered IMC crystals here largely nucleated on the largest TiB_2 particles. This is consistent with a relatively high energy barrier for nucleation of ordered, faceted compounds and the difficulty of kinetic attachment of atoms onto the crystal facets, related to their higher entropy of fusion [53, 54]. Solute suppression of any of the largest TiB_2 led to less nucleation of the IMCs (Figs. 10 and 11). For relatively easy-to-form, disordered α -Al crystals, solute suppression effects can activate more, smaller nucleants, but for difficult-to-form, ordered IMC crystals which rely exclusively on the largest, most efficient nucleants, solute suppression tends to reduce the overall number of crystals.

Compared with earlier work on Fe-rich IMCs [30], the stronger X-ray absorption contrast provided by the Pt-rich IMCs here enabled detection of the crystals at

their early formation stage, time-resolved nucleation bursts, and resolution of the associated solute depletion. The interdependence between the final IMC number density and the nucleation bursts, i.e. an intense single burst for isothermal conditions or multiple, less intense bursts for directional conditions were differentiated. Overall, the trends here for IMCs relating to the effects of thermal gradient, cooling rate, size and magnitude of the *ANZ* and solute suppression support the models originally developed based on disordered solid solution phases [11, 55, 56].

In real castings, IMCs usually form as secondary phases towards the later stage of solidification when only a minority of liquid remains, and the local formation environment is therefore different from the primary nucleation conditions used here to facilitate imaging. It is known that finely dividing this residual liquid, for example by feathery grains and ideally suppressing its inter-connectivity before IMCs appear, helps to refine advantageously the IMC population [57]. Although there is no doubt a potent geometric aspect to this effect – IMCs cannot grow large in small isolated pockets of near-eutectic composition liquid – our results suggest that there will also be a strong solute effect: once one or a few IMCs are formed, the majority of the residual liquid in an inter-dendritic pocket will be under solute suppressed conditions and the chances of another nucleation event vanishingly small. Geometric and solute effects thus explain why usually only one IMC is observed in each eutectic pocket [49, 58]. In addition, measurement of the IMC number density suggests that only a very small proportion ($\sim 0.5\%$) of TiB_2 particles in the melt were efficient nucleants to nucleate IMCs. Therefore, if more efficient IMC nucleants can be developed and added to the melt, and flat temperature gradients facilitated, then nucleation bursts would be favoured, leading to a possible further refinement of IMCs in commercial Al castings.

5 Conclusions

The nucleation of primary Pt-rich $\text{Al}_{24}\text{Pt}_9\text{Er}_4$ crystals was studied as an analogue for the behaviour of $\text{Al}_{13}\text{Fe}_4$ in commercial Al alloys, providing strong X-ray absorp-

tion contrast allowing early detection of IMC formation from the liquid, resolution
of the associated Pt diffusion fields and quantification of the Pt-depleted liquid frac-
tion. IMC formation behaviour was investigated during directional and isothermal
solidification when the alloy was inoculated with TiB_2 using *in situ* synchrotron
X-ray radiography. With 4,037 IMCs studied in 12 experiments over a wide range
of cooling rate, the key findings were:

1. The nucleation of the primary Pt-rich IMCs proceeded in distinct bursts (in
the time domain) or waves (in the spatial domain), the magnitude of which
increased with increasing cooling rate at a given thermal gradient. The isother-
mal solidification led to the highest magnitude of burst for a given cooling rate.
2. For a given thermal gradient, the average crystal formation rate increased
linearly with increasing cooling rate, whereas the IMC number density first
increased rapidly as cooling rate increased from 0.1 Ks^{-1} to 0.5 Ks^{-1} and
then remained approximately constant up to 8 Ks^{-1} . The weak sensitivity of
the Pt-rich IMC number density to higher cooling rates was consistent with
earlier measurements performed on $\text{Al}_{13}\text{Fe}_4$. Comparing the maximum Pt-rich
IMC number density with the estimated TiB_2 number density suggested that
IMC crystals nucleated principally only on the most potent nucleant particles,
including TiB_2 with diameters $>6 \mu\text{m}$ and, potentially, potent oxide particles.
3. Estimation of the available undercooling in front of a growing IMC crystal
revealed the dominant effect of thermal gradient on the size of the active
nucleation zone (ANZ), which determined the number of potent nucleants
available to catalyse IMC nucleation at each instant. Isothermal cooling de-
veloped the largest ANZ and therefore gave rise to the largest IMC number
density with potent nucleants activated in a single burst. Under directional
cooling, both the ANZ and the maximum available undercooling were reduced
at low growth velocity (i.e. low cooling rate) but were less sensitive to increas-
ing velocity, which explained the weak dependency of IMC number density on
higher cooling rates.

4. Time-resolved measurements of the Pt-depleted liquid fraction suggested a competition between the ongoing nucleation of new crystals and the growth/coarsening of existing crystals. By applying a higher cooling rate, and more importantly isothermal conditions, the growth of IMCs was effectively constrained, and more IMC crystals were able to nucleate before solute depletion of the entire liquid volume suppressed the probability of further IMC nucleation.
5. Considering an ensemble of potential nucleants and IMC crystals and their interaction in the melt, it is suggested that the probability of IMC nucleation at any time instant, assuming equal potency of all nucleants, depends on the number of IMCs already formed and the fraction of liquid solute depleted.
6. Refinement of IMCs in commercial alloys might be achieved if nucleation bursts can be facilitated by adding more efficient IMC nucleants and imposing flat thermal gradients.

Acknowledgements

This work was supported by EPSRC (UK) under grant number EP/N007638/1 (Future Liquid Metal Engineering Hub). This work was enabled by synchrotron beamtime ID 19 at European Synchrotron Radiation Facility (Experiment No. MA4063).

References

- [1] B. S. Murty, S. A. Kori, M. Chakraborty, Grain refinement of aluminium and its alloys by heterogeneous nucleation and alloying, *Int. Mater. Rev.* 47 (1) (2002) 3–29.
- [2] J. C. Fisher, J. H. Hollomon, D. Turnbull, Nucleation, *J. Appl. Phys.* 19 (8) (1948) 775–784.
- [3] D. Turnbull, J. C. Fisher, Rate of nucleation in condensed systems, *J. Chem. Phys.* 17 (1) (1949) 71–73.

- [4] D. Turnbull, Kinetics of heterogeneous nucleation, *J. Chem. Phys.* 18 (2) (1950) 198–203.
- 535 [5] J. H. Hollomon, D. Turnbull, Nucleation, *Prog. Met. Phys.* 4 (C) (1953) 333–388.
- [6] D. Turnbull, Theory of catalysis of nucleation by surface patches, *Acta Metall.* 1 (1) (1953) 8–14.
- 540 [7] I. Maxwell, A. Hellawell, A simple model for grain refinement during solidification, *Acta Metall.* 23 (2) (1975) 229–237.
- [8] B. Cantor, R. D. Doherty, Heterogeneous nucleation in solidifying alloys, *Acta Metall.* 27 (1) (1979) 33–46.
- [9] A. L. Greer, A. M. Bunn, A. Tronche, P. V. Evans, D. J. Bristow, Modelling of inoculation of metallic melts: application to grain refinement of aluminium by Al-Ti-B, *Acta Mater.* 48 (11) (2000) 2823–2835.
- 545 [10] D. Shu, B. Sun, J. Mi, P. S. Grant, A quantitative study of solute diffusion field effects on heterogeneous nucleation and the grain size of alloys, *Acta Mater.* 59 (5) (2011) 2135–2144.
- [11] D. H. Stjohn, M. Qian, M. A. Easton, P. Cao, The Interdependence Theory: The relationship between grain formation and nucleant selection, *Acta Mater.* 59 (12) (2011) 4907–4921.
- 550 [12] A. Buffet, H. N. Thi, A. Bogno, T. Schenk, N. Mangelinck-Noel, G. Reinhart, N. Bergeon, B. Billia, J. Baruchel, Measurement of solute profiles by means of synchrotron X-ray radiography during directional solidification of Al-4 wt% Cu alloys, *Mater. Sci. Forum* 649 (January) (2010) 331–336.
- 555 [13] A. Bogno, H. Nguyen-Thi, A. Buffet, G. Reinhart, B. Billia, N. Mangelinck-Noël, N. Bergeon, J. Baruchel, T. Schenk, Analysis by synchrotron X-ray radiography of convection effects on the dynamic evolution of the solid–liquid

- interface and on solute distribution during the initial transient of solidification,
 560 Acta Mater. 59 (11) (2011) 4356–4365.
- [14] G. Reinhart, N. Mangelinck-Noël, H. Nguyen-Thi, T. Schenk, J. Gastaldi,
 B. Billia, P. Pino, J. Härtwig, J. Baruchel, Investigation of columnar–equiaxed
 transition and equiaxed growth of aluminium based alloys by X-ray radiogra-
 phy, Mater. Sci. Eng. A 413 (2005) 384–388.
- 565 [15] R. H. Mathiesen, L. Arnberg, P. Bleuet, A. Somogyi, Crystal fragmentation
 and columnar-to-equiaxed transitions in Al-Cu studied by synchrotron X-ray
 video microscopy, Metall. Mater. Trans. A 37 (8) (2006) 2515–2524.
- [16] Q. Dong, J. Zhang, J. Dong, H. Xie, Z. Li, Y. Dai, Y. Liu, B. Sun, In situ
 observation of columnar-to-equiaxed transition in directional solidification us-
 570 ing synchrotron X-radiation imaging technique, Mater. Sci. Eng. A 530 (2011)
 271–276.
- [17] D. Ruvalcaba, R. H. Mathiesen, D. G. Eskin, L. Arnberg, L. Katgerman, In situ
 observations of dendritic fragmentation due to local solute-enrichment during
 directional solidification of an aluminum alloy, Acta Mater. 55 (13) (2007)
 575 4287–4292.
- [18] E. Liotti, A. Lui, R. Vincent, S. Kumar, Z. Guo, T. Connolley, I. P. Dolbnya,
 M. Hart, L. Arnberg, R. H. Mathiesen, P. S. Grant, A synchrotron X-ray radio-
 graphy study of dendrite fragmentation induced by a pulsed electromagnetic
 field in an Al–15Cu alloy, Acta Mater. 70 (2014) 228–239.
- 580 [19] E. Liotti, A. Lui, S. Kumar, Z. Guo, C. Bi, T. Connolley, P. S. Grant, The
 spatial and temporal distribution of dendrite fragmentation in solidifying Al-Cu
 alloys under different conditions, Acta Mater. 121 (2016) 384–395.
- [20] T. Nelson, B. Cai, N. Warnken, P. Lee, E. Boller, O. Magdysyuk, N. Green,
 Gravity effect on thermal-solutal convection during solidification revealed by

- 585 four-dimensional synchrotron imaging with compositional mapping, *Scr. Mater.*
180 (2020) 29–33.
- [21] A. Bogno, H. Nguyen-Thi, G. Reinhart, B. Billia, J. Baruchel, Growth and
interaction of dendritic equiaxed grains: In situ characterization by synchrotron
X-ray radiography, *Acta Mater.* 61 (4) (2013) 1303–1315.
- 590 [22] A. G. Murphy, W. U. Mirihanage, D. J. Browne, R. H. Mathiesen, Equiaxed
dendritic solidification and grain refiner potency characterised through in situ
X-radiography, *Acta Mater.* 95 (2015) 83–89.
- [23] A. Murphy, R. Mathiesen, Y. Houltz, J. Li, C. Lockowandt, K. Henriksson,
G. Zimmermann, N. Melville, D. Browne, XRMON-SOL: Isothermal equiaxed
595 solidification of a grain refined Al–20 wt%Cu alloy, *J. Cryst. Growth* 440 (2016)
38–46.
- [24] A. Prasad, S. D. McDonald, H. Yasuda, K. Nogita, D. H. StJohn, A real-
time synchrotron X-ray study of primary phase nucleation and formation in
hypoeutectic Al-Si alloys, *J. Cryst. Growth* 430 (2015) 122–137.
- 600 [25] Y. Jia, H. Huang, Y. Fu, G. Zhu, D. Shu, B. Sun, D. StJohn, An in situ investi-
gation of the solute suppressed nucleation zone in an Al-15Cu alloy inoculated
by Al-Ti-B, *Scr. Mater.* 167 (2019) 6–10.
- [26] E. Liotti, C. Arteta, A. Zisserman, A. Lui, V. Lempitsky, P. S. Grant, Crystal
nucleation in metallic alloys using x-ray radiography and machine learning, *Sci.*
605 *Adv.* 4 (4) (2018) eaar4004.
- [27] J. A. Taylor, Iron-Containing Intermetallic Phases in Al-Si Based Casting Al-
loys, *Procedia Mater. Sci.* 1 (2012) 19–33.
- [28] G. Sha, K. A. Q. O’Reilly, B. Cantor, J. M. Titchmarsh, R. Hamerton, Quasi-
peritectic solidification reactions in 6xxx series wrought Al alloys, *Acta Mater.*
610 51 (7) (2003) 1883–1897.

- [29] S. Ji, W. Yang, F. Gao, D. Watson, Z. Fan, Effect of Iron in Al-Mg-Si-Mn Ductile Diecast Alloy, *Light Met.* 2013 (2013).
- [30] S. Feng, E. Liotti, A. Lui, M. D. Wilson, T. Connolley, R. H. Mathiesen, P. S. Grant, In-situ X-ray radiography of primary Fe-rich intermetallic compound formation, *Acta Mater.* 196 (2020) 759–769.
- [31] V. M. T. Thiede, B. Fehrmann, W. Jeitschko, Ternary Rare Earth Metal Palladium and Platinum Aluminides R4Pd9Al24 and R4Pt9Al24, *Zeitschrift fur Anorg. und Allg. Chemie* 625 (9) (1999) 1417–1425.
- [32] J. Grin, U. Burkhardt, M. Ellner, K. Peters, Refinement of the Fe4Al13 structure and its relationship to the quasihomological homeotypical structures, *Zeitschrift fuer Krist.* 209 (6) (1994) 479–487.
- [33] M. D. Wilson, R. Cernik, H. Chen, C. Hansson, K. Iniewski, L. L. Jones, P. Seller, M. C. Veale, Small pixel CZT detector for hard X-ray spectroscopy, *Nuclear Instruments and Methods in Physics Research, Section A: Accelerators, Spectrometers, Detectors and Associated Equipment* 652 (1) (2011) 158–161.
- [34] P. Seller, S. Bell, R. J. Cernik, C. Christodoulou, C. K. Egan, J. A. Gaskin, S. Jacques, S. Pani, B. D. Ramsey, C. Reid, P. J. Sellin, J. W. Scuffham, R. D. Speller, M. D. Wilson, M. C. Veale, Pixellated Cd(Zn)Te high-energy X-ray instrument, *J. Instrum.* 6 (12) (2011) 12009–12009.
- [35] M. C. Veale, S. J. Bell, D. D. Duarte, A. Schneider, P. Seller, M. D. Wilson, K. Iniewski, Measurements of charge sharing in small pixel CdTe detectors, *Nucl. Instruments Methods Phys. Res. Sect. A Accel. Spectrometers, Detect. Assoc. Equip.* 767 (2014) 218–226.
- [36] E. Liotti, A. Lui, T. Connolley, I. P. Dolbnya, K. J. S. Sawhney, A. Malandain, M. D. Wilson, M. C. Veale, P. Seller, P. S. Grant, Mapping of multi-elements during melting and solidification using synchrotron X-rays and pixel-based spectroscopy, *Sci. Rep.* 5 (2015) 6.

- [37] M. C. Veale, P. Seller, M. Wilson, E. Liotti, HEXITEC: A High-Energy X-ray Spectroscopic Imaging Detector for Synchrotron Applications, Synchrotron Radiat. News 31 (6) (2018) 28–32.
- [38] S. Feng, E. Liotti, M. D. Wilson, L. Jowitt, P. S. Grant, In situ mapping of chemical segregation using synchrotron x-ray imaging, MRS Bull. 45 (11) (2020) 934–942.
- [39] A. L. Greer, Overview: Application of heterogeneous nucleation in grain-refining of metals, J. Chem. Phys. 145 (21) (2016) 211704.
- [40] A. L. Greer, Grain refinement of alloys by inoculation of melts, Philos. Trans. R. Soc. London. Ser. A Math. Phys. Eng. Sci. 361 (1804) (2003) 479–495.
- [41] T. Quested, A. Greer, The effect of the size distribution of inoculant particles on as-cast grain size in aluminium alloys, Acta Mater. 52 (13) (2004) 3859–3868.
- [42] X. Cao, J. Campbell, The nucleation of Fe-Rich phases on oxide films in Al-11.5Si-0.4Mg cast alloys, Metall. Mater. Trans. A 34 (7) (2003) 1409–1420.
- [43] X. Cao, J. Campbell, The solidification characteristics of Fe-rich intermetallics in Al-11.5Si-0.4Mg cast alloys, Metall. Mater. Trans. A 35 (5) (2004) 1425–1435.
- [44] D. N. Miller, L. Lu, A. K. Dahle, The role of oxides in the formation of primary iron intermetallics in an Al-11.6Si-0.37Mg alloy, Metall. Mater. Trans. B Process Metall. Mater. Process. Sci. 37 (6) (2006) 873–878.
- [45] S. Terzi, J. A. Taylor, Y. H. Cho, L. Salvo, M. Suery, E. Boller, A. K. Dahle, In situ study of nucleation and growth of the irregular α -Al/ β -Al₅FeSi eutectic by 3-D synchrotron X-ray microtomography, Acta Mater. 58 (16) (2010) 5370–5380.

- [46] C. Puncreobutr, A. B. Phillion, J. L. Fife, P. Rockett, A. P. Horsfield, P. D. Lee, In situ quantification of the nucleation and growth of Fe-rich intermetallics during Al alloy solidification, *Acta Mater.* 79 (2014) 292–303.
- [47] Z. Song, O. V. Magdysyuk, L. Tang, T. Sparks, B. Cai, Growth dynamics of faceted Al₁₃Fe₄ intermetallic revealed by high-speed synchrotron X-ray quantification, *J. Alloys Compd.* 861 (2021) 158604.
- [48] J. Rakhmonov, G. Timelli, F. Bonollo, Influence of Melt Superheat, Sr Modifier, and Al-5Ti-1B Grain Refiner on Microstructural Evolution of Secondary Al-Si-Cu Alloys, *Metall. Mater. Trans. A Phys. Metall. Mater. Sci.* 47 (11) (2016) 5510–5521.
- [49] A. Lui, P. S. Grant, I. C. Stone, K. A. Q. O'Reilly, The Role of Grain Refiner in the Nucleation of AlFeSi Intermetallic Phases During Solidification of a 6xxx Aluminum Alloy, *Metall. Mater. Trans. A* 50 (11) (2019) 5242–5252.
- [50] W. Tiller, K. Jackson, J. Rutter, B. Chalmers, The redistribution of solute atoms during the solidification of metals, *Acta Metall.* 1 (4) (1953) 428–437.
- [51] Y. Xu, D. Casari, R. H. Mathiesen, Y. Li, Revealing the heterogeneous nucleation behavior of equiaxed grains of inoculated Al alloys during directional solidification, *Acta Mater.* 149 (2018) 312–325.
- [52] R. Corless, G. Gonnet, D. Hare, D. Jeffrey, D. Knuth, On the lambert w function, *Advances in Computational Mathematics* 5 (1996) 329–359.
- [53] K. Jackson, D. Uhlmann, J. Hunt, On the nature of crystal growth from the melt, *J. Cryst. Growth* 1 (1) (1967) 1–36.
- [54] C. M. Adam, L. M. Hogan, Crystallography of the Al-Al₃ Fe eutectic, *Acta Metall.* 23 (3) (1975) 345–354.
- [55] W. Winegard, B. Chalmers, Supercooling and dendritic freezing in alloys, *Trans. Am. Soc. Met.* 46 (1954) 1214–1224.

- 690 [56] D. H. StJohn, A. Prasad, M. A. Easton, M. Qian, The Contribution of Constitutional Supercooling to Nucleation and Grain Formation, *Metall. Mater. Trans. A* 2015 4611 46 (11) (2015) 4868–4885.
- [57] S. Kumar, K. A. Q. O'Reilly, Influence of Al grain structure on Fe bearing intermetallics during DC casting of an Al-Mg-Si alloy, *Mater. Charact.* 120 (2016) 311–322.
- 695 [58] S. Ji, Y. Wang, D. Watson, Z. Fan, Microstructural evolution and solidification behavior of Al-Mg-Si alloy in high-pressure die casting, *Metall. Mater. Trans. A Phys. Metall. Mater. Sci.* 44 (7) (2013) 3185–3197.